State-to-State Transport in Hypersonic Entry Flows

Ana Catarina Garbacz Gomes
ana.g.gomes@tecnico.ulisboa.pt

Instituto Superior Técnico, Universidade de Lisboa, Portugal

September 2018

Abstract

This work studies nonequilibrium hypersonic flows surrouding space reentry vehicles. The design of such vehicles and its thermal protection systems relies on the accurate modelling of transport phenomena. For this purpose, dissociation and vibrational energy transfer relaxation processes are treated using a vibrational state-to-state kinetics approach. A numerical study is carried out to assess the impact of using state-specific transport coefficients in CFD simulations of hypersonic external flowfields. Two transport models have been considered in the code SPARK: the Gupta-Yos/CCS macroscopic model directly transposed to state-to-state species, and the same model considering enchanced state-dependent collisional cross-sections. The code was applied to a full Navier-Stokes simulation of a nitrogen flow past a sphere. The obtained results were compared against the following simulations: Euler state-to-state, Navier-Stokes one-temperature and two-temperature simulations. Accounting for transport phenomena in a state-to-state approach resulted in smoother variations of the flow properties, translated into a 15% lower peak temperature and a significantly thicker shock layer. Comparing to the two-temperature simulation, the state-to-state approach yielded, respectively, a 10% and 5% larger shock standoff distance and peak temperature. Nonetheless, the impact of the enchanced state-dependent cross-section model was found to be negligible. The effects of dissociation and vibrational excitation processes were confirmed to be emphasised for higher freestream temperatures.

Keywords: Reentry, Hypersonic, Transport, State-to-state

1. Introduction

Sample return and manned space exploration missions include a superorbital reentry into Earth's atmosphere, during which the vehicle may reach speeds up to 13 km/s (the Stardust sample return capsule was the fastest man-made object to reenter Earth's atmosphere at 12.9 km/s [1]). Under these conditions, a strong and high-temperature (up to 10^4-10^5 K) shockwave is formed. In order to withstand the nonequilibrium aerothermodynamic environment that results from such high temperatures, reentry capsules are designed as a blunt-body favouring shock detachment. The detachment of the shock leaves room between the shock and the thermal protection system (TPS) surface, where a series of fast and complex endothermic physico-chemical processes occur, allowing to cool the shock layer and minimizing the resulting convective and radiative heat fluxes at the vehicle's surface. Hence, the accurate assessment of the surface heat flux is of paramount importance for the design of the TPS.

To that end, computational fluid dynamics (CFD) simulations play a major role. The accurate prediction of the reentry flow properties requires the modelling of a large number of gas dynamics processes, such as translation-vibration exchange processes, dissociation and ionization, as well as the modelling of transport properties (mass diffusion, viscosity and thermal conductivity). For this purpose, the most commonly used approaches are multi-temperature models and state-to-state kinetics. The latter takes into account internal levels population distributions different from the Boltzmann equilibrium distribution, upon which multi-temperature models are based on.

1.1. State-of-the-art

In the multi-temperature approach, Park's two temperature model is the most widely used in Navier-Stokes solvers [2, 3, 4, 5, 6]. Scalabrin and Boyd [2], Hao et al. [4] and Loureiro [6] compared the effect of both transport models Wilke/Blottner/Eucken and Gupta-Yos/CCS mixing rules by simulating axssymetric reentry flows. Results provided by the two models were in good agreement with flight data, although the Gupta-Yos/CCS model yielded better results for higher entry speeds (for which ionization becomes significant).

By considering a more general state-to-state approach, it has been shown that highly non-Boltzmann vibrational distributions are indeed found in the stagnation region of a hypersonic nitrogen flow past a blunt-body [7]. Within this framework, state-to-state inviscid reentry simulations have been carried out [8, 9, 10, 11, 12, 13] . It was concluded that state-to-state outcomes may help explain known disagreements with experimental findings, when resorting to multi-temperature models. Nevertheless, the estimation of convective heat fluxes requires taking diffusion processes into account. Yet, the coupling of fluid dynamic equations to transport coefficients obtained on the basis of the state-to-state kinetic theory suffers from huge computational costs. Very few Navier-Stokes simulations have accounted for state-specific quantum distributions and the consideration of diffusive fluxes has traditionally been achieved by means of post-processing [14, 15, 16, 17]. One-dimensional studies allowed to conclude that, under strong nonequilibrium conditions, state-to-state vibrational kinetics significantly impacts transport properties [18] as well as fluid dynamic variables and heat fluxes [19, 20, 21]. Moreover, Kustova has claimed that the effect for accounting for vibrational excitation in collisional cross-sections is mostly negligible[22].

The present work aims at providing the first groundwork for the inclusion of a full state-specific transport model in the governing fluid dynamic equations. Two transport models – the Gupta-Yos/CCS macroscopic model directly transposed to state-to-state species, and the same model considering enchanced state-dependent collisional cross-sections – are implemented in a CFD code with the objective of simulating a full state-to-state Navier-Stokes simulation of a nitrogen flow past a sphere. Further, the following simulations are carried out for comparison purposes: one-temperature and two-temperature Navier-Stokes simulations with macroscopic Gupta-Yos/CCS transport model (considering Boltzmann distributions) and Euler state-to-state. For the sake of simplicity, ionization is neglected and only vibrational energy levels are considered.

2. Physical Models and Mathematical Formulation

Hypersonic viscous flows are described by the Navier-Stokes conservation equations. To include nonequilibrium effects, one mass conservation equation 1a is defined for each species s, accounting for the production and destruction of the species in the source term $\dot{\omega}_s$ and for mass diffusion terms. The momentum equation 1b enforces Newton's Second Law. The total energy equation 1c constitutes the conservation of energy.

$$\frac{\partial(\rho c_s)}{\partial t} + \vec{\nabla}.(\rho c_s \vec{u}) = \vec{\nabla}.\vec{J_s} + \dot{\omega}_s \tag{1a}$$

$$\frac{\partial(\rho \vec{u})}{\partial t} + \vec{\nabla}.(\rho \vec{u} \otimes \vec{u}) = \vec{\nabla}.[\tau] - \vec{\nabla} p \tag{1b}$$

$$\frac{\partial(\rho E)}{\partial t} + \vec{\nabla}.(\rho E \vec{u}) = \vec{\nabla}.\Big(\sum_k \vec{q}_{c_k} + \sum_s \vec{J}_s h_s + \vec{u}.[\tau] - p\vec{u} \Big) \tag{1c}$$

In Eqs. 1a-1c, s denotes species, ρ is the density, $\vec{u}$ the mean velocity in vectorial form, c_s the mass fraction, $\vec{J_s}$ the mass diffusion flux, $\dot{\omega}_s$ the chemical source term, $[\tau]$ the viscous stress tensor, p the pressure, E the total energy, $q_{\vec{c_k}}$ the conduction heat flux of energy mode k and h_s the enthalpy.

2.1. Chemical Kinetic Models

In the equation for mass conversation of each species s (Eq. 1a), the kinetic source term $\dot{\omega}_s$ concerns the mass production/destruction rate of each species s and is determined by a chemical-kinetic model. It depends on the reversible chemical reactions occuring in the flow and the respective chemical rates. A generic elementary reaction R (a reaction that takes place in a single step) is defined as follows:

$$\sum_{s=1}^{NS} \nu'_s x_s \underset{K_b}{\overset{K_f}{\rightleftharpoons}} \sum_{s=1}^{NS} \nu''_s x_s \tag{2}$$

where x_s is the molar fraction of species s, ν'_s is the stoichiometric coefficient for reactant s, ν''_s is the stoichiometric coefficient for product s, K_f is the forward rate constant and K_b is the backward rate constant.

K_f and K_b are not independent, instead they are related through the so-called detailed balance principle through the equilibrium constant K_{eq}:

$$\frac{K_f}{K_b} = K_{eq} \tag{3}$$

where K_{eq} is related to the equilibrium chemical concentrations and may be determined from the reactant and product species partition functions, both in the conditions of thermal equilibrium and nonequilibrium.

The forward rate constants are usually measured experimentally for a given temperature range and fitted to an Arrhenius equation:

$$K_f = A T^{-n} \exp\left(-\frac{\theta_r}{T} \right) \tag{4}$$

where A, n and θ_r are respectively a constant, the pre-exponential factor and the temperature of reaction.

The kinetic source term $\dot{\omega}_s$ is then defined as:

$$\dot{\omega}_s = M_s \sum_R (\nu''_{sr} - \nu'_{sr}) \left[K_{f_R} \prod_s x_s^{\nu'_{sr}} - K_{b_R} \prod_s x_s^{\nu''_{sr}} \right] \tag{5}$$

where M_s is the molar mass of species s and the index R stands for a given reaction.

2.1.1 State-to-State Kinetics

As previously discussed, state-specific models treat each internal level as a pseudo-species, allowing the determination of more accurate non-Boltzmann distributions for entry flows. Among other more detailed (yet computationally intensive) models, the Forced Harmonic Oscillator (FHO) theory has been utilized quite successfully [23], yielding physically consistent vibrational state-specific rates K_f and K_b that accurately reproduce thermal dissociation rates in the Boltzmann equilibrium limit. This semiclassical model considers the excitation of an harmonic oscillator by another body as it approaches and moves away from the oscillator, allowing the determination of the probabilities of transition from one vibrational level to another. Multiquantum, vibrationally-specific rates are then obtained as function of transition probabilities considering a Maxwellian velocity distribution function, for kinetic mechanims of the following types:

- Vibration-Translation (V–T)

$$\mathrm{AB(v)+M} \rightarrow \mathrm{AB(v+\Delta v)+M} \tag{6}$$

- Vibration-Vibration-Translation (V–V–T)

$$\mathrm{AB(v)+AB(w)} \rightarrow \mathrm{AB(v+\Delta v)+AB(w+\Delta w)} \tag{7}$$

- Vibration-Dissociation (V–D)

$$\mathrm{AB(v)+M} \rightarrow \mathrm{A+B+M} \tag{8}$$

where v and w denote different vibrational levels. The equations that provide the transition probabilities for each case can be found in Ref. [24].

2.2. Transport Models

Transport phenomena is introduced in the dissipative terms of Eqs. 1a-1c , which are defined as function of the corresponding gradients and transport coefficients:

$$\vec{J_s} = \rho D_s \vec{\nabla}(c_s) \tag{9}$$

$$[\tau] = \mu\Big(\vec{\nabla}\vec{u} + (\vec{\nabla}\vec{u})^T\Big) - \frac{3}{2}\mu\Big(\vec{\nabla}.\vec{u}\Big)[I] \tag{10}$$

$$\vec{q}_{c_k} = \lambda_k \vec{\nabla}(T_k) \tag{11}$$

where D_s is the mass diffusion coefficient of species s, μ is the mixture viscosity coefficient and λ_k is the thermal conductivity coefficient of energy mode k.

In the following subsections the two models used in the frame of this work and based on the Gupta–Yos theory are presented.The general model, transposed for state-specific species is discussed in section 2.2.1 and the model with enchanced vibrationally-specific coliisional cross-sections is presented in section 2.2.2.

2.2.1 Gupta–Yos/Collision Cross-Section - Model 0

The Gupta-Yos/CCS model [25] is an approximate mixing rule that provides the transport coefficients for the chemical species, on the basis of Boltzmann distributions. It accounts for the true nature of the viscosity collision integrals by considering the corresponding collision cross-sections. In order to couple this model to a state-resolved kinetic scheme, it was considered that the transport coefficients of each sub-species v/w were equal to the transport coefficients of the corresponding chemical species s/r:

$$D_{sr_{vw}} = D_{sr} \tag{12}$$

$$\mu_{s_v} = \mu_s \tag{13}$$

$$\lambda_{k,s_v} = \lambda_{k,s} \tag{14}$$

where $D_{sr_{vw}}$ is the mass diffusion coefficient between sub-species v and w and D_{sr} the mass diffusion coefficient between the corresponding chemical species species s and r, respectively. μ_{s_v} and λ_{k,s_v} are the viscosity and thermal conductivity, respectively, of each sub-species v, μ_s and $\lambda_{k,s}$ are the viscosity and thermal conductivity, respectively, of the corresponding chemical species s.

The strength of the interaction between each pair of species (s,r) is given by the collision terms ${\Delta_{sr}}^{(1)}$ and ${\Delta_{sr}}^{(2)}$ as function as the controlling temperature T_c:

$$\Delta_{sr}^{(1)} = \frac{8}{3}\left[\frac{2M_sM_r}{\pi R_u T_c(M_s+M_r)}\right]^{1/2} \pi{\overline{\Omega}_{sr}}^{(1,1)}(T_c)\times 10^{20} \tag{15}$$

$$\Delta_{sr}^{(2)} = \frac{16}{5}\left[\frac{2M_sM_r}{\pi R_u T_c(M_s+M_r)}\right]^{1/2} \pi{\overline{\Omega}_{sr}}^{(2,2)}(T_c)\times 10^{20} \tag{16}$$

where $\pi{\overline{\Omega}_{sr}}^{(1,1)}$ and $\pi{\overline{\Omega}_{sr}}^{(2,2)}$ represent weighted averages of the cross-sections, which are evaluated as curve fits to the tabular data generated in [26]. The controlling temperature T_c in equations (15) and (16) depends on the type of particles colliding. It refers to the heavy-species translational temperature $T_{tra,h}$, except if the collision involves an electron, in which case the electron temperature $T_{exc} = T_{tra,el}$ should be used.

The expressions for the species transport coefficients μ_s, $\lambda_{s,k}$ and D_s provided by this model are function of of the collision terms ${\Delta_{sr}}^{(1)}$, ${\Delta_{sr}}^{(2)}$ and can be found in Ref. [6].

2.2.2 Gupta–Yos with State-Dependent Collisional Cross-Section - Model 1

The State-Dependent Collisional Cross-Section Model is a simplified state-specific transport model. This is a more detailed method than the previous one, since it accounts for the influence of variable molecular diameters when the molecules are vibrationally excited. It considers the formulation of the Gupta-Yos/CCS model and additionally accounts for the enhancement of the average collision cross-sections $\overline{\Omega}_{sr}^{(1,1)}$ and $\overline{\Omega}_{sr}^{(2,2)}$ according to:

$$\overline{\Omega}_{vw}^{(1,1)} = \overline{\Omega}_{sr}^{(1,1)} \times \frac{\Omega_{CD(w)}^{AB(v)}}{\Omega_{CD(eq)}^{AB(eq)}} \tag{17}$$

$$\overline{\Omega}_{sr}^{(2,2)} = \overline{\Omega}_{sr}^{(2,2)} \times \frac{\Omega_{CD(w)}^{AB(v)}}{\Omega_{CD(eq)}^{AB(eq)}} \tag{18}$$

where $\Omega_{CD(w)}^{AB(v)}$ is the hard-sphere collisional cross-section between the (v) vibrational level of diatom AB and the (w) vibrational level of diatom CD, $\Omega_{CD(eq)}^{AB(eq)}$ is the equilibrium hard-sphere collisional cross-section between diatoms AB and CD.
For diatom-diatom collisions, we have:

$$\Omega_{CD(w)}^{AB(v)} = \pi \Big(\frac{\sigma_v^{AB} + \sigma_w^{CD}}{2} \Big)^2 \tag{19}$$

For atom-diatom collisions, we have:

$$\Omega_{CD(w)}^{AB(v)} = \pi \Big(\frac{\sigma_v^{AB} + \sigma^{C}}{2} \Big)^2 \tag{20}$$

In equation 20, σ is the interaction distance, which equals the sum of the internuclear distance and the electron cloud distance:

$$\sigma^{AB(v)} = r_v^{AB} + (\sigma_{eq}^{AB} - r_{eq}^{AB}) \tag{21}$$

where r_{eq}^{AB} is the internuclear distance of the molecule in equilibrium, σ_{eq}^{AB} is the low-velocity interaction distance and r_v^{AB} is the internuclear distance of the vibrational energy levels. Regarding the N_2/N mixture studied in this work, since N(1) is not a molecular sub-species, $\sigma^{AB(v)}$ and σ_{eq}^{AB} are the same: $\sigma^{AB(v)} = \sigma_{eq}^{AB}$.

3. Implementation

The transport models presented in the previous section were implemented in the SPARK code, maintained at IPFN. This code includes both the Euler and the Navier-Stokes formulations, for which the numerical resolution is achieved by the cell-centered finite-volume method. Both second-order explicit and implicit time integration schemes are available for temporal discretization. With regard to spatial discretization, diffusive fluxes are discretized using standard second-order central finite-differences. Convective terms are discretized on the basis of Roe's approximate Riemann solver, using the second-order Harten-Yee scheme [27]. Variables are evaluated at the cell's faces with Roe averages between the left and right states. Furthermore, in order to avoid numerical oscillations the minmod flux limiter is applied to characteristic variables.

3.1. Numerical Setup

3.1.1 0D Equilibrium Computations

0D equilibrium computations were conducted to perform verification on the implemented models, and compare them against those already implemented in SPARK. Model 0 and Model 1 vibrational state-specific models were compared to Wilke/Blottner/Eucken and Gupta-Yos/CCS macroscopic models (based on Boltzmann distributions). For each case, transport coefficients were computed as function of the temperature, using equilibrium concentrations of the species for a N_2/N mixture, at atmospheric pressure and a range of temperatures between 500 K and 50,000 K. Results for the thermal conductivity coefficient are presented and discussed in Section 4.1, in order to help understand and discuss results obtained in multidimensional simulations.

3.1.2 Multidimensional Simulations

To assess the impact of the implemented transport models on reentry flows, a mixture consisting of 61 vibrational levels for the N_2 molecule and 1 electronic level for atomic nitrogen N was considered. Seven different simulations were performed for a two-dimensional flow past a sphere with radius $r = 0.1524$ m, at v=7 km/s and pressure 27 kPa:

- **Model 0:** full state-to-state Navier-Stokes simulation using the Gupta-Yos transport model adapted to state-specific species (section 2.2.1) for $T_\infty = 300$ K and $T_\infty = 700$ K.
- **Model 1:** full state-to-state Navier-Stokes simulation using the state-specific Gupta-Yos transport model with enchanced state-specific collisional cross-sections (section 2.2.2) for $T_\infty = 300$ K and $T_\infty = 700$ K.
- **Euler:** a full state-to-state Euler simulation for $T_\infty = 300$ K.

- **1T:** one-temperature Navier-Stokes simulation using Gupta-Yos transport model (macroscopic) for $T_\infty = 300$ K.

- **2T:** two-temperature Navier-Stokes simulation using Gupta-Yos transport model (macroscopic) for $T_\infty = 300$ K.

3.2. Mesh and Boundary Conditions

Given the axisymmetry condition of the problem and since it is assumed that the convective heat fluxes are negligible in the low-density afterbody region (a reasonable assumption shared by the works presented in the state-of-the-art), only half of the front body was considered in the computational domain. Figure 1 shows the boundary conditions considered in all simulations performed in this work.

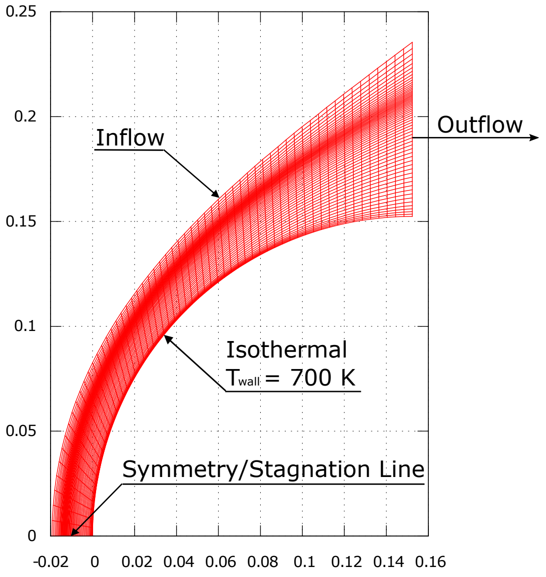

Figure 1: Boundary conditions considered for the CFD domain

4. Results and Discussion

4.1. Transport Model Assessment

Results obtained for the equilibrium composition of the N_2/N mixture as function of the temperature have shown that: (a) there is no dissociation of N_2 for $T < 4{,}000$ K, (b) for $T < 11{,}000$ K, N_2 becomes completely dissociated, (c) from $T = 4{,}000$ K up to $T = 11{,}000$ K, N_2 molar fraction decreases while N molar fraction naturally increases and (d) at $T = 6{,}000$ K, both N_2 and N molar fractions are 0.5. This value ($T = 6{,}000$ K) of the gas temperature will be important in the analysis of the thermal conductivity coefficient evolution with temperature, shown in Fig. 2.

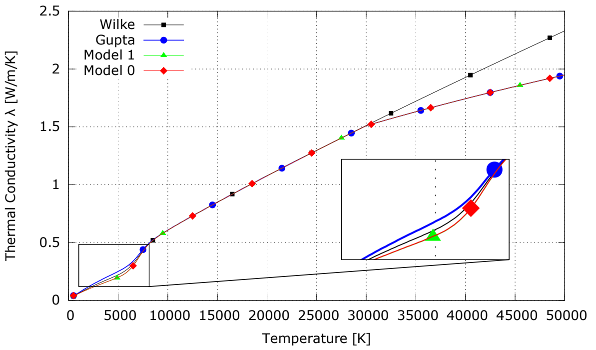

Figure 2: Comparison of transport models: mixture thermal conductivity coefficient λ.

For $8{,}000 < T < 30{,}000$ K, the four methods all compute approximately the same value for thermal conductivity. For $T > 30{,}000$ K, results determined by Wilke's mixing rule begin to significantly overpredict the thermal conductivity coefficient comparing to the other methods. This is likely due to Wilke's assumption that all interactions between any particles present the same (hard sphere) cross-section.

For $T < 8{,}000$ K, the Eucken relation (Wilke), Gupta's mixing rule and Model 0 yield slightly different results. This difference is more prominent for temperatures around 6000 K, which coincides with the temperature for which N_2 and N concentrations equilibrate.

Up to approximately $T = 8{,}000$ K, Gupta's mixing rule yields a slightly higher conductivity than Wilke's mixing rule and both of these results are slightly higher than those provided by Model 0. The decrease in thermal conductivity of Model 0 relative to Gupta's mixing rule is due to the fact that, for N_2, the vibrational contribution for the thermal conductivity vanishes in a state-to-state approach, in which vibrational energy is not function of the temperature. This difference is no longer observable for $T > 8{,}000$ K since, in that case, the thermal conductivity coefficient is only due to the concentration of N, for which the contribution to the global coefficient remains the same in the state-to-state and macroscopic description (only the translational contribution is present in both).

For the whole temperature range, one can conclude that taking into account the increased size of $N_2(v)$ vibrational levels (Model 1) does not impact the mixture thermal conductivity coefficient, since the curves for Model 0 and Model 1 are coincident. The impact of Model 1 also turned out to be negligible in terms of viscosity and mass diffusion.

4.2. Application Case: Flow Over a Sphere

4.2.1 Impact of Transport Model

Figure 3 shows the translational temperature T and the equivalent vibrational temperature T_{vib} for the five test-cases: 1T, 2T, Euler, Model 0 and Model 1. The shock position, indicated by the peak region, is located at, approximately: x = -10.5 mm for Euler, Model 0 and Model 1; x = -9.5 mm for 2T; x = -9 mm for 1T. The maximum shock temperatures are, respectively: 21,000 K, 18,000 K, 18,000 K, 17,000 K and 14,000 K.

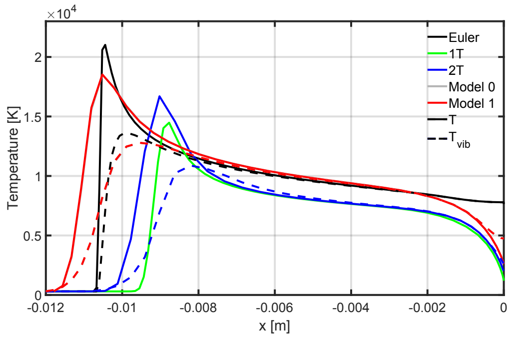

Figure 3: Comparison of transport models for T_∞ = 300 K: Stagnation line temperature.

The differences between shock standoff distances and peak temperature values are expectable since, in the state-to-state approach (Euler, Model 0, Model 1), endothermic vibrational relaxation is slower and the translational temperature accordingly decreases in a slower fashion (as seen in fig. 3). The gas density will be lower and the gas will expand to a larger shock standoff distance. This is further emphasized in the one-temperature case (1T) where essentially the energy tranfer to the vibrational mode is instantaneous, since $T_{tr} = T_{vib}$.

With regard to the Navier-Stokes state-to-state simulations, there are no differences between Model 0 and Model 1. This is predictable given the results presented in Section 4.1.

Comparing the sharp shock-layer temperature gradients of the Euler simulation to those resulting from Model 0/Model 1, we observe that mass diffusion effects (considerably enchanced by the species gradients from the reactive chemistry behind the bow-shock wave - see Fig. 4) significantly even out temperature gradients: the peak temperature value for Model 0/Model 1 is 15% lower than the one predicted in Euler and the shock layer is significantly thicker in the former case. This smaller translational temperature peak will have a considerable impact on the radiative properties of the shock layer, since radiation is, on a first approach, T^4 dependent (Planck's black-body law). Radiation source terms in the case of the Navier-Stokes results will accordingly be lower than those of the Euler results.

Furthermore, focusing on the results provided by the four viscous simulations (1T, 2T, Model 0, Model 1), the translational and vibrational temperatures tend to equilibrate in the boundary layer, to the same values of the 1T simulation. This is expectable since state-to-state and 1T/2T Boltzmann Navier-Stokes models are expected to converge to the same results for the macroscopic conditions that favour a Boltzmann equilibrium – large Damkhohler numbers (which define the ratio of the flow time scale to the chemical time scale). However, this is not completely achieved, especially in the case of Model 0 and Model 1 simulations: the equivalent vibrational temperature T_{vib} starts to deviate from the remaining curves approximately at x = -0.5 mm, and at x = 0 mm T_{vib} is 30% higher than T. This may be explained by insufficient mesh refinement near the wall, or insufficient time marching of the solution[1] Comparing to Model 0/Model 1, the temperature at x = 0 mm is about 50% lower for 1T and 40% lower for 2T, which results in a higher wall convective heat flux for the Navier-Stokes state-to-state simulations.

In the case of the Euler simulation, refinement in the boundary layer is not essential since the wall is, by definition, adiabatic - which translates in the absence of temperature gradients typically found in a boundary layer. Accordingly, the two temperatures T and T_{vib} start to perfectly converging at x = -4 mm.

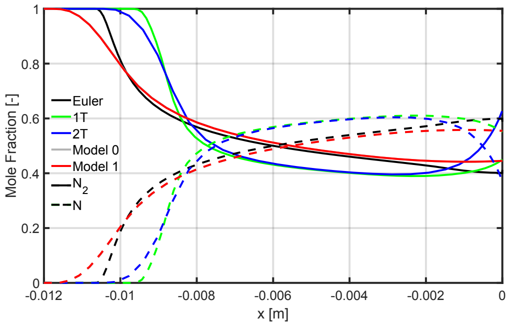

Figure 4: Comparison of transport models for T_∞ = 300 K: Stagnation line mole fractions of chemical species N_2 and N.

Figure 4 presents the mole fractions of chemical species N_2 and N. Apart from the boundary layer region, the obtained curves show a similar behaviour. In the upstream region only N_2 molar fractions are found. As soon as the temperature rises - which happens for different positions in the stagnation line

---

[1] since attempts to reach CFL numbers higher than about 0.01 by switching to an implicit flow model were not successful

depending on the simulation under consideration - dissociation reactions begin to occur, causing the molar fractions of atomic nitrogen to gradually increase and, in reverse, molecular nitrogen fractions to decrease. With respect to Model 0 and Model 1, once again the impact of the latter turns out to be completely negligible (coincident curves).

Analysing the region where dissociation starts to occur, there are some noteworthy differences between the different models. In the case of viscous simulations, reactions initiate at x = -11.5 mm for Model 0 and Model 1, at x = -10.5 mm for 2T and, lastly, at x = -10 mm for 1T. This is consistent with the different shock positions associated with each simulation (see Fig. 3), which is expectable since dissociation reactions are activated by the corresponding high-temperatures. Comparing the Euler state-to-state simulation to the Navier-Stokes state-to-state simulations (Model 0 and Model 1), the only difference is the enhanced smothness in the latter case, explained by the presence of mass diffusion processes.

Focusing on the boundary layer region, recombination effects are clearly noticeable in the case of both multi-temperature simulations (denoted by the increase/decrease in the molar fractions of N_2/N). This phenomenon is more enhanced in the case of the 2T simulation, for which the N_2 molar fraction is 30% higher than for 1T, contrary to what was expected. Again, this might be the consequence of insufficiently converged simulation in terms of time or mesh.

In the case of state-to-state simulations, there is no recombination at the wall for the inviscid results (adiabatic condition). For Model 0/Model 1, there are very slight recombination effects near the surface of the vehicle. This is not obvious when observing the graph, once again since the new state of equilibrium appears not to be properly captured by the mesh. However, this was verified through analysis of the output data. At x = 0 mm, there is about 10% more N_2 for Model 0 than for Euler. This difference is due to mass diffusion effects, since recombination is negligible in Model 0.

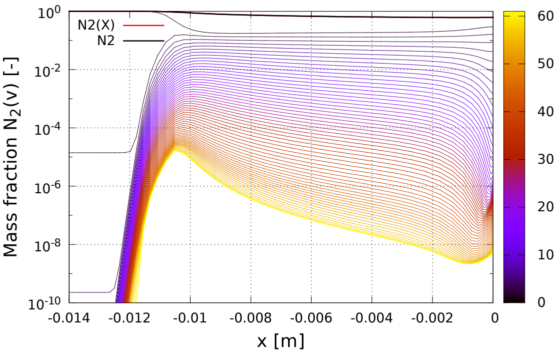

(a) Model 0.

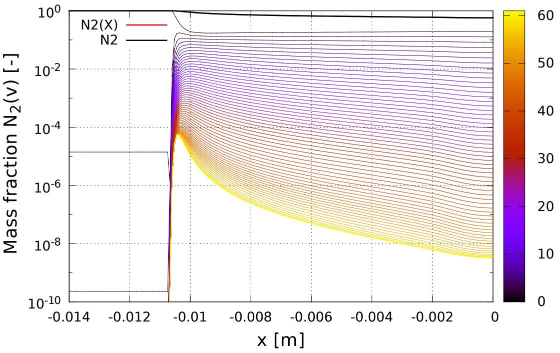

(b) Euler.

Figure 5: Comparison between Euler and Navier-Stokes state-to-state simulations for T_∞ = 300K: mass fractions of $N_2(v)$ vibrational levels along the stagnation line.

Figure 5 presents the mass fraction of each vibrational level along the stagnation line, for both the Euler and Model 0 simulations. For each case, right before the temperature peak region, there is a significant increase in the population of all the upper vibrational levels of N_2, at the expense of the $v = 0$ level, caused by the high increase in the shock wave temperature. Shortly after the temperature peak, around x = -10.5 mm, dissociation of N_2 takes over and all the energy levels start being depleted more or less evenly. This means that multiquantum transitions between different levels are as dominant as monoquantum transitions.

Comparing both figures, the mass diffusion effects present in Model 0 are evident. This is clear along the entire stagnation line, where the curves resulting from Model 0 are much smoother than those resulting from Euler. Furthermore, around x = -1 mm, we see a drastic increase of the population of higher $N_2(v)$ levels, in Model 0. This occurs because the flow reaches the boundary layer with about a 55% degree of dissociation, and the sudden temperature decrease in the boundary layer will lead to a strongly recombining flow, favouring recombination in the upper levels. In the Euler simulation, on the other hand, no gradients are observed in x = 0 mm, which, once again, is explained by the absence of a boundary layer.

4.2.2 Impact of Freestream Temperature

Figure 6 shows the stagnation line temperature of Model 0 and Model 1 for $T_\infty = 700$ K and of Model 0 for $T_\infty = 300$ K.

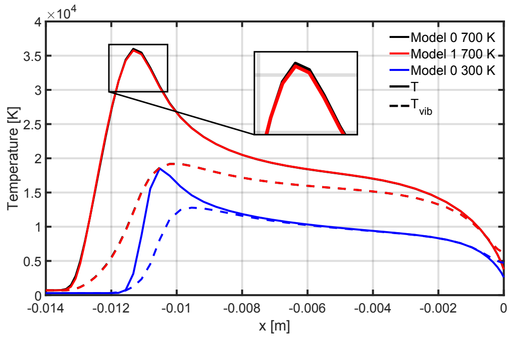

Figure 6: Impact of the freestream temperature: Stagnation line temperature for Model 0 and Model 1 at $T_\infty = 700$ K and for Model 0 at $T_\infty = 300$ K.

Comparing results provided by the different freestream temperatures, generally a similar behaviour is observed. The shock standoff distance is about 10% larger for $T_\infty = 700$ K. Also for this case, the peak temperature value is about 50% higher than for $T_\infty = 300$ K. These two main differences are explained by the fact that higher freestream velocities (a consequence of a higher freestream temperature, since $V_\infty = M_\infty \times \sqrt{\gamma R T_\infty}$) lead to a more energetic flow.

Additionally, for $T_\infty = 700$ K the curve of the translational temperature is moderatly smoother in the peak region, where temperature gradients are larger. This is indicative of a more adequate mesh refinement in the shock-layer than for the case of $T_\infty = 300$ K.

Furthermore, for $T_\infty = 700$ K, the impact of accounting for increased cross-sections of vibrational levels (Model 1) is negligible, similarly to what was concluded for $T_\infty = 300$ K. However, zooming in the peak temperature for $T_\infty = 700$ K, it is slightly higher for Model 0 than for Model 1, while for $T_\infty = 300$ K both curves were coincident along the whole stagnation line (see Fig. 3). This may be attributed to two factors: (a) better mesh refinement for $T_\infty = 700$ K; (b) since, for $T_\infty = 700$ K, temperatures reach much higher values, the corresponding gradients will be larger and diffusion phenomena will be enhanced. It is found that accounting for larger effective cross-sections (Model 1) results in a more diffusive flow, compared to Model 0.

Nevertheless, for $T_\infty = 700$ K, refinement in the boundary layer region is still insufficient. Similarly to the case of $T_\infty = 300$ K, equilibrium is not achieved near the sphere's surface, since results of T_{vib} deviate from those of T for about 25% in the case of $T_\infty = 700$ K, at x = 0 mm. Moreover, for $T_\infty = 700$ K, the translational temperature is 30% higher than for $T_\infty = 300$ K at the wall, resulting in a higher convective heat flux, which is consistent with the fact that the flow is more energetic in the former case.

The impact of freestream temperature on stagnation line mole fractions of chemical species is studied in Fig. 7. Model 0 is compared to Model 1 for $T_\infty = 700$ K and $T_\infty = 700$ K is compared to $T_\infty = 300$ K for Model 0.

For $T_\infty = 700$ K, there are no differences between Model 0 and Model 1, which is expected given the results presented in the previous two figures. Analysing the impact of the freestream temperature for Model 0, there are considerable differences between the two cases. For $T_\infty = 700$ K, dissociation reactions start to occur sooner - around x = -13 mm for $T_\infty = 700$ K and x = -12 mm for $T_\infty = 300$ K -, which is consistent with the corresponding shock standoff distances. Moreover, dissociation effects are significantly more enhanced for $T_\infty = 700$ K - approximately 99% of atomic nitrogen at the wall for $T_\infty = 700$ K against 55% for $T_\infty = 300$ K. This is expectable since higher temperatures tend to favour dissociation.

Nonetheless, in the boundary layer region, recombination effects are almost nonexistent. As observed in Fig. 6, equilibrium conditions are not reached near the wall, pfor the same reasons as discussed before

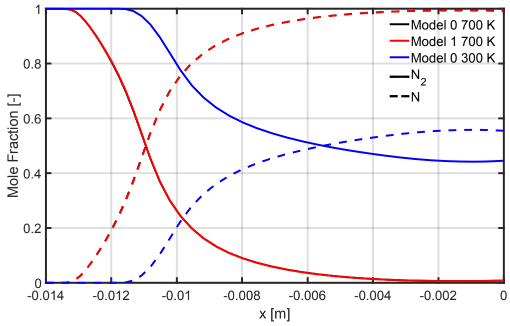

Figure 7: Impact of freestream temperature: stagnation line mole fractions of chemical species N_2 and N - Model 0 and Model 1 at $T_\infty = 700$ K and Model 0 at $T_\infty = 300$ K.

Figure 8 shows the vibrational distribution functions of $N_2(v)$ for different positions along the stagnation line, comparing $T_\infty = 700$ K against $T_\infty = 300$ K with Model 0. Mass fractions of vibrational levels $N_2(v)$ are normalized solely to the N_2 mass fraction (excluding N). As the distance from

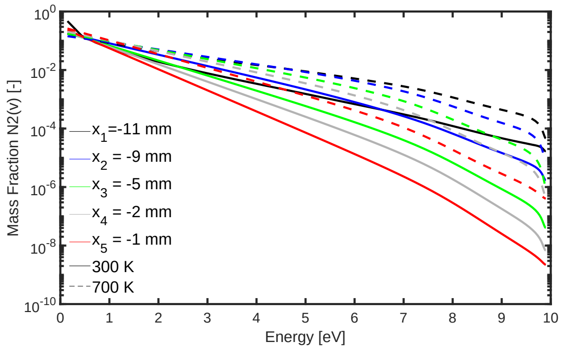

Figure 8: Vibrational distribution functions of $N_2(v)$ for different positions along the stagnation line: T_∞ = 700 K vs. T_∞ = 300 K for Model 0.

the wall decreases, concentrations of vibrational levels are increasingly higher for more energetic levels, in the case of T_∞ = 700 K. This is expectable, since higher temperatures favour molecular vibrational excitation. In the boundary layer region (x = -1 mm) the flow time scales increase significantly due to a decrease in velocity. Consequently, a Boltzmann equilibrium is almost reached (Boltzmann distributions are translated into straight lines in a log plot).

5. Conclusions

A better understanding of the nonequilibrium processes experienced by a space vehicle during reentry into Earth was provided. High-speed reentry is characterized by strong nonequilibrium conditions, under which state-to-state vibrational kinetics are found to significantly impact the transport properties of the gas in the shock layer.

In light of this, a successfull full state-to-state Navier-Stokes simulation was performed for a nitrogen flow over a sphere. In order to account for transport phenomena and non-Boltzmann distributions over the vibrational levels, two simplified state-specific transport models were employed: Model 0 was formulated as a direct adaptation of the macroscopic Gupta-Yos/CCS model to state-to-state species. The more detailed Model 1 followed the same formulation, however accounting for the increased cross-sections of vibrationally excited molcules in the collision terms. For comparison purposes, multi-temperature Navier-Stokes and Euler state-to-state simulations were performed as well.

As expected, a comparison between multi-temperature and state-to-state approaches resulted in a significantly more energetic flow for the latter case, translated into larger shock standoff distances and higher peak temperatures (respectively, 10% and 5% larger than for the two-temperature case). However, results provided by the state-to-state Navier-Stokes simulations did not converge to the same temperature profiles than those provided by multi-temperature simulations at the wall, where equilibrium conditions are expected to be encountered. It was concluded that more rigorous mesh refinement or time convergence is necessary in this region, so as to capture the steep gradients occuring in the boundary layer.

Simulations using state-specific transport coefficients resulted in smoother variations for the flow properties comparing to the Euler case: a significantly thicker shock-layer and a 15% lower peak temperature. A comparison between Model 0 and Model 1 allowed confirming that the coupled effect of vibrational molecular size and non-Boltzmann distributions on the transport properties is negligible, and does not impact the flowfield.

The impact of the freestream temperature (translated into freestream velocity) was evaluated for 300 and 700 K (7 and 10.7 km/s for the same Mach number, respectively). For the higher freestream temperature, the effects of microscopic thermochemical processes such as dissociation and vibrational excitation are emphasised. Moreover, there is a slight influence of the cross-section effective size in the peak temperature, but is still considered to be negligible.

These findings will have a remarkable impact on the design of TPS systems, since they not only provide a better estimation of the flow properties but allow a more accurate prediction of radiative heat fluxes as well, which depend on the temperature field provided by CFD simulations.

Acknowledgements

I gratefully acknowledge the support of Prof. Mário Lino da Silva, Dr. Maria Castela and Dr. Bruno Lopez for the success of the present work.

References

[1] P. Desai, D. Lyons, J. Tooley, and J. Kangas. Entry, descent, and landing operations analysis for the stardust entry capsule. *Journal of Spacecraft and Rockets*, 45(6):1262–1268, 2008.

[2] L. C. Scalabrin and I. D. Boyd. Numerical simulations of the FIRE-II convective and radiative heating rates. AIAA Paper 2007-4044, 2007.

[3] H. S. Massimia, H. Shen, C. Y. Wen, Y. S. Chen, and S. M. Liang. Numerical analysis of hypersonic flows around blunt-nosed models and a space vehicle. *Aerospace Science and Technology*, 43:360–371, 2015.

[4] J. Hao, J. Wang, and C. Lee. Numerical study of hypersonic flows over reentry configurations with different chemical nonequilibrium models. *Acta Astronautica*, 126:1–10, 2016.

[5] J. Hao, J. Wangb, Z. Gaoa, C. Jianga, and C. Leea. Comparison of transport properties models for numerical simulations of mars entry vehicles. *Acta Astronautica*, 130:24–33, 2017.

[6] D. Loureiro. High-temperature modeling of transport properties in hypersonic flows. Master's thesis, Instituto Superior Técnico, 2015.

[7] G. V. Candler, J. Olejniczak, and B. Harrold. Detailed simulation of nitrogen dissociation in stagnation regions. *Physics of Fluids*, 9:2108–2117, 1997.

[8] E. Nagnibeda. The structure of the relaxation zone behind shock waves in the reacting gas flows. Aerothermodynamics for Space Vehicles, ESA SP 367, ESA Publication Division, ESTEC, Noordwijk, The Netherlands, pp. 299–303, 1995.

[9] F. Lordet, J. Meolans, A. Chauvin, and R. Brun. Nonequilibrium vibration-dissociation phenomena behind a propagating shock wave: Vibrational population calculation. *Shock Waves*, 4:299–312, 1995.

[10] I. Adamovich, S. Macheret, J. Rich, and C. Treanor. Vibrational energy transfer rates using a forced harmonic oscillator model. *Journal of Thermophysics and Heat Transfer*, 12(1):57–65, 1998.

[11] S. Ruffin and C. Park. Vibrational relaxation of anharmonic oscillators in expanding flows. AIAA Paper 92–0806, 1992.

[12] G. Colonna, M. Capitelli, M. Tuttafesta, and D. Giordano. Non-arrhenius no formation rate in one-dimensional nozzle airflow. *Journal of Thermophysics and Heat Transfer*, 13(3):372–375, 1999.

[13] I. Armenise, M. Capitelli, G. Colonna, and C. Gorse. Nonequilibrium vibrational kinetics in the boundary layer of re-entering bodies. *Journal of Thermophysics and Heat Transfer*, 10(3):397–405, 1996.

[14] E. Josyula, W. F. Bailey, and K. Xu. Nonequilibrium relaxation in high speed flows. AIAA Paper 2004-2468, 2004.

[15] E. Josyula, J. M. Burt, and K. Xu. Influence of thermochemical nonequilibrium on transport properties for hypersonic flow simulations. AIAA Paper 2012-3191, 2012.

[16] E. Josyula, J. M. Burt, E. Kustova, and M. Mekhonoshina. State-to-state kinetic modeling of dissociating and radiating hypersonic flows. AIAA Paper 2015-0475, 2015.

[17] E. Josyula, J. M. Burt, E. Kustova, and P. Vedula. Influence of state-to-state transport coefficients on surface heat transfer in hypersonic flows. AIAA Paper 2014-0864, 2014.

[18] D. Bruno, M. Capitelli, E. Kustova, and E. Nagnibeda. Non-equilibrium vibrational distributions and transport coefficients of $N_2(v)$/–N mixtures. *Chemical Physics Letters*, 308:463–472, 1999.

[19] O. Kunova, E. V. Kustova, M. Mekhonoshina, and E. Nagnibeda. The influence of state-to-state kinetics on diffusion and heat transfer behind shock waves. AIP Conference Proceedings 1628, 1202 (2014).

[20] E. V. Kustova and E. A. Nagnibeda. Transport properties of a reacting gas mixture with strong vibrational and chemical nonequilibrium. *Chemical Physics*, 233:57–75, 1998.

[21] O. Kunova, E. V. Kustova, M. Mekhonoshina, and E. Nagnibeda. Non-equilibrium kinetics, diffusion and heat transfer in shock heated flows of N_2/N and O_2/O mixtures. *Chemical Physics*, 463:70–81, 2015.

[22] E. Kustova and G. M. Kremer. Influence of state-to-state vibrational distributions on transport coefficients of a single gas. AIP Conference Proceedings 1786, 070002 (2016).

[23] M. Lino da Silva, V. Guerra, and J. Loureiro. State-resolved dissociation rates for extremely nonequilibrium atmospheric entries. *Journal of Thermophysics and Heat Transfer*, 21(1):40–49, 2007.

[24] B. Lopez, M. Lino da Silva, V. Guerra, and J. Loureiro. Coupled hydrodynamic/state- specific high-temperature modeling of nitrogen vibrational excitation and dissociation. *Journal of Thermophysics and Heat Transfer*, AIAA Paper 2013-1585484, 2013.

[25] P. Gnoffo, R. N. Gupta, and J. L. Shinn. Conservation equations and physical models for hypersonic air flows in thermal and chemical nonequilibrium. Technical report, NASA, 1989.

[26] F. G. Blottner, M. Johnson, and M. Ellis. Chemically reacting viscous flow program for multi- component gas mixtures. Technical report, Sandia Laboratories, 1971.

[27] B. Lopez. *Simulation des Ecoulements de Plasma Hypersonique Hors Equilibre Thermochimique*. PhD thesis, Université D'Orléans, France, 2010.